## PAPER

Check for updates

# 3D porous Li₃V₂(PO₄)₃/hard carbon composites for improving the rate performance of lithium ion batteries

Zhaoyang Wang, [iD] [a] Wen He,*[ab] Xudong Zhang,*[a] Xinli Yi,[a] Jichao Wang, [iD] [a] Guihua Yang[b] and Yuanzheng Yue[ac]

In this paper, three dimensional (3D) porous Li₃V₂(PO₄)₃ (LVP)/hard carbon (HC) composites have been synthesized *via* a simple method at 800 °C. The XRD, SEM, HRTEM, XPS, Raman spectra, TG, and BET show that the 3D LVP/HC composite is composed of monoclinic LVP nanocrystals (50–100 nm in size) and 3D HC (about 9 wt%) with a pore size range of 2–200 nm. The LVP nanoparticles were conglutinated and uniformly coated by HC. We have clarified the formation mechanism of the nanocomposite structure and the influences of the calcination temperature on the structure and electrochemical properties of 3D porous LVP/HC composites. As a novel cathode for lithium ion batteries, the 3D LVP/HC composites exhibit desired electrochemical performances with a discharge capacity of 143 mA h g⁻¹ at the rate of 0.1C and excellent cycle stability at high rate (the retention capacity is about 92 mA h g⁻¹ after 1000 cycles at 10C).

## 1. Introduction

In recent years, electric vehicles (EVs) and hybrid electric vehicles (HEVs) have become the key to solve the energy problem.[1–4] To achieve this goal, batteries with high power and energy, low cost, long cycle life, environmental compatibility and good security are urgently needed. Monoclinic Li₃V₂(PO₄)₃ (LVP) has attracted considerable interest since it can be used in fabricating lithium ion battery cathodes with high cell-voltage, robust structure and suitable theoretical specific capacity (133 mA h g⁻¹ for extraction of two lithium ions when cycled between the potential window of 3.0 V and 4.3 V *vs.* Li/Li⁺).[5,6] Despite these advantages, its low electronic conductivity (2.4 × 10⁻⁷ S cm⁻¹ at room temperature) is still a problem for LVP, which greatly limits its rate performance and application in high power batteries.[7–9] To solve this problem, several strategies including coating with conductive materials[10] and metal ion doping[11] have been used.

A carbon coating is widely used to improve the electronic conductivity.[12–15] The hard carbon (HC) material with randomly oriented graphitic layers can deliver a capacity of *ca.* 300 mA h g⁻¹ and act as a good conductive medium for charge transmission, and thus it is a promising material for LIBs, SIBs and

supercapacitors. Here, we develop the LVP modified with three dimensional (3D) porous hard carbon network macrostructure. This 3D architecture can provide 3D interconnected network of both electron and ion pathways,[16–18] which can greatly enhance the electrochemical performance. Moreover, the carbon coating layer also acts as a protective layer between the LVP cathode and the electrolyte, suppressing the corrosion of LVP particles by the electrolyte.[19,20] Unfortunately, 3D porous hard carbon is difficult to be fabricated at a large scale, not only because of their high cost, but also the complexity in the process of preparation.

With the rapid development of glass fiber industry, the challenge for treatment of glass fiber lubricant wastewater (GFLW) produced from the fiber-drawing process has limited the sustainable development of glass fiber industry. If GFLW with a high chemical oxygen demand (CODcr) was discharged directly into the environment, it not only pollutes environment, destroys ecology and loses economy, but also threatens human survival and health. Because GFLW is an emulsion with high dispersion and stability, and its chemical composition is very complicated, which contains lubricant, emulgator, lipid, dissolved organic matter and so on, its recovery is expensive and difficult to be treated. Here, we propose a simple way to tackle this environmental problem by turning GFLW into high-performance hard carbon material. Using GFLW as structure template and carbon resource, we have synthesized the LVP/HC composites with three-dimensional (3D) porous structure, which exhibit extraordinary electrochemical performances. The GFLW is found to be a promising raw material for fabricating cost-effective, environmentally friendly, high performance lithium ion batteries (LIBs). This greatly contributes to reducing

[a] *College of Material Science and Engineering, Qilu University of Technology, Jinan 250353, China. E-mail: hewen1960@126.com; zxd1080@126.com; yy@bio.auu.dk; Fax: +86 531 89631518; Tel: +86 531 89631080*

[b] *Key Laboratory of Pulp and Paper Science and Technology of Ministry of Education, Qilu University of Technology, Jinan 250353, China*

[c] *Section of Chemistry, Aalborg University, DK-9000 Aalborg, Denmark*

the GFLW load to our environment and the synthetic cost of LIBs, thus accelerating its market penetration.

## 2. Experimental

### 2.1. Synthesis of nanocomposites

The nanocomposites were prepared *via* sol–gel reactions assisted by impregnating compound template. The raw materials used in this experiment include $NH_4VO_3$ (99%, Tianjin Kermel Chemical Reagent Co., Ltd), $Li_2CO_3$ (97%, Tianjin Damao Chemical Co., Ltd), $C_2H_2O_4 \cdot 2H_2O$ (99.5%, Tianjin Bodi Chemical Co., Ltd), $NH_4H_2PO_4$ (99.0%, Tianjin Guangfu Technology Development Co., Ltd) and glass fibre drawing wastewater (GFLW). Distilled water was used during the synthesis of the samples.

The $Li_3V_2(PO_4)_3/C$ nanocomposites were synthesized by sol–gel process. 0.02 mol $NH_4VO_3$ and $C_2H_2O_4 \cdot 2H_2O$ were dissolved into 100 ml GFLW solution with stirring at 80 °C for 0.5 h (molar ratio of $NH_4VO_3/C_2H_2O_4 \cdot 2H_2O = 2:3$). After the formation of a clear blue $VOC_2O_4$ precursor solution, the $NH_4H_2PO_4$ and $Li_2CO_3$ were added into the above solution (molar ratio of Li : V : P = 3 : 2 : 3) with stirring last for 0.5 h. The mixed solution was continuously stirred till gel formation and then dried at 100 °C in an air oven. The resulting mixtures were sintered at 350 °C for 5 h in nitrogen atmosphere, the obtained brown intermediate product followed by grinding, then the powder calcination at 750/800/850 °C for 8 h in nitrogen atmosphere, final product are marked as LVP/C-1, LVP/HC-2 and LVP/C-3, respectively. The pure LVP was also prepared at 800 °C for comparison.

### 2.2. Material characterization

The crystal phase composition of the synthesized samples were confirmed by X-ray diffraction (XRD) employing a Cu-Kα X-ray diffractometer (PANalytical X'Pert PRO; Netherlands). The diffraction patterns were collected over a diffraction angle $2\theta$ range of 10–70° with a scan rate of 6° per min. The morphologies and element mappings of synthesized samples were investigated by scanning electron microscopy (SEM) and high-resolution transmission electron microscope (HRTEM). The property of carbon was analyzed with a Renishaw In-Via Raman microscopic instrument equipped with an $Ar^+$ laser ($\lambda = 785$ nm) at $50\times$ aperture. Thermogravimetric analysis (TGA) of the samples was conducted in air at a heating rate of 10 °C $min^{-1}$ from ambient to 1000 °C using a thermal analyzer (TGA1 STAR System) in order to measure the carbon content. The specific surface area and Barrett–Joyner–Halenda (BJH) pore size distribution was carried out at 77 K using an automatic surface area analyzer (Micromeritics, Gemini V2380, USA) under continuous adsorption conditions.

### 2.3. Electrochemical tests

To make electrodes, 80% active materials were mixed with 10% acetylene black and 10% poly-vinylidene fluoride (PVDF) in *N*-methyl pyrrolidone (NMP) to ensure homogeneity. Then the mixture was coated on aluminum foil with a thickness about 0.02 mm, dried under the air atmosphere at 60 °C for 3 h and vacuum atmosphere at 120 °C for 12 h and cut into circular strips of 15 mm in diameter. CR 2032 coin cells were assembled in a glove box filled with high-purity argon. The electrolyte was composed of 1 M $LiPF_6$ dissolved in dimethyl carbonate (DMC)/ethylene carbonate (EC)/ethylene methyl carbonate (EMC) with a volume ratio of 1 : 1 : 1. Lithium metal and polypropylene film were employed as anode and separator, respectively. Before galvanostatic charging/discharging test, the cells were aged for more than 12 h to ensure full absorption of the electrolyte into the electrodes. The galvanostatic charging/discharging tests were carried out in the voltage range of 3.0 V to 4.3 V at different current densities on channels battery analyzer (CT3008W). The cyclic voltammetry (CV) and electrochemical impedance (EIS) tests were performed on a PARSTAT 2263 electrochemical workstation. The voltage range of the CV measurements was 3.0–4.3 V and the scanning rate was from 0.1 to 5 mV $s^{-1}$. The impedance data were recorded in the frequency range from 0.1 MHz to 10 mHz and AC signal of 5 mV in amplitude as the perturbation. All the tests were performed at room temperature.

## 3. Result and discussion

Fig. 1 is the schematic illustration of the synthesis route for the LVP/HC sample. There is a large number of surface-active substances, such as bisphenol A epoxy resin (BAER) in GFLW. Fig. 1a and b show the chemical structure of BAER, including hydrophobic groups (nonpolar tail groups with the red curve said in Fig. 1c) and hydrophilic groups (polar head with blue acanthosphere said in Fig. 1c). When the $NH_4VO_3$ and $C_2H_2O_4 \cdot 2H_2O$ were dissolved into 100 ml GFLW solution, the $VO^{2+}$ combined with the hydrophilic group of BAER by means of electrostatic adsorption (Fig. 1d). As the reaction temperature increases, the mixed solution is concentrated. When it gets to the critical micelle concentration, the BAER molecules in the solution self-assemble to form spherical micelles. $VO^{2+}$ ions were adsorbed evenly on the surface of the micelles (as show in Fig. 1e). Further concentration, the spherical micelles contact with each other to form a gelate (Fig. 1f). After calcination in a $N_2$ protection atmosphere, the gelate was carbonized to form the 3D porous LVP/HC composites as shown in Fig. 1g.

The morphology and structure of samples prepared under different synthesis conditions were systematically characterized by SEM and HRTEM. From SEM image in Fig. 2a, it is seen that the LVP/HC-2 sample is constituted by the particles with various shapes, such as polygonal grains, porous particles, triangular rods and so on. Fig. 2b shows that the porous size range of LVP/HC-2 particle is 20–200 nm. Fig. 2c is the TEM image of LVP/HC-2 sample, showing that the size of LVP nanoparticles (black particle) is about 50–100 nm and the LVP nanoparticles were conglutinated and uniformly coated by porous hard carbon (light color net). The HRTEM image (Fig. 2d) displays the LVP skeleton structure and non-uniform pores (*i.e.*, pores with different shapes and a broad distributions of diameters) (indicated by white spots) in LVP/HC-2 sample. Fig. 2e shows the crystal lattice spacings of 0.36 nm which matchs well with the (130) plane of monoclinic $Li_3V_2(PO_4)_3$. From Fig. 2f we can more
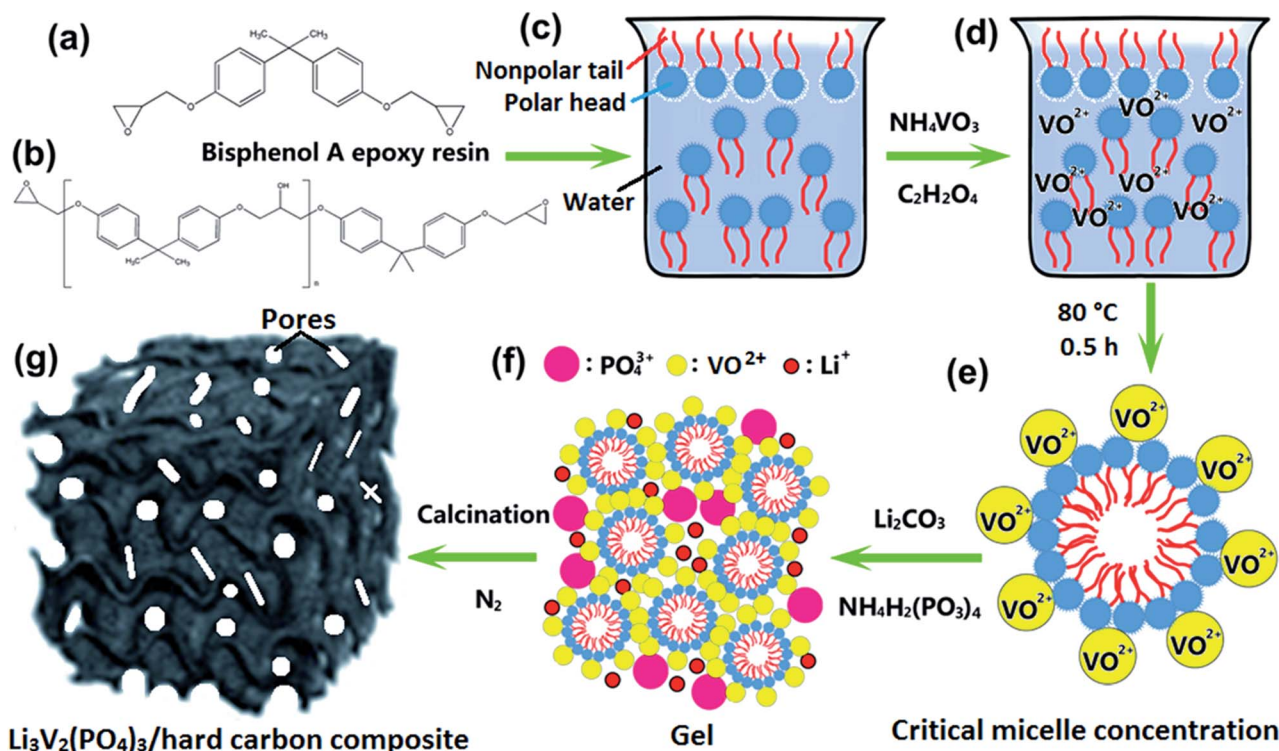
Fig. 1 Synthesis mechanism of nanocomposite. (a and b) Monomer and the polymer of BAER. (c) GFLW as solvent. (d–f) Reveal the adsorption effect of BAER on the material. (g) The structure diagram of the sample after calcination.
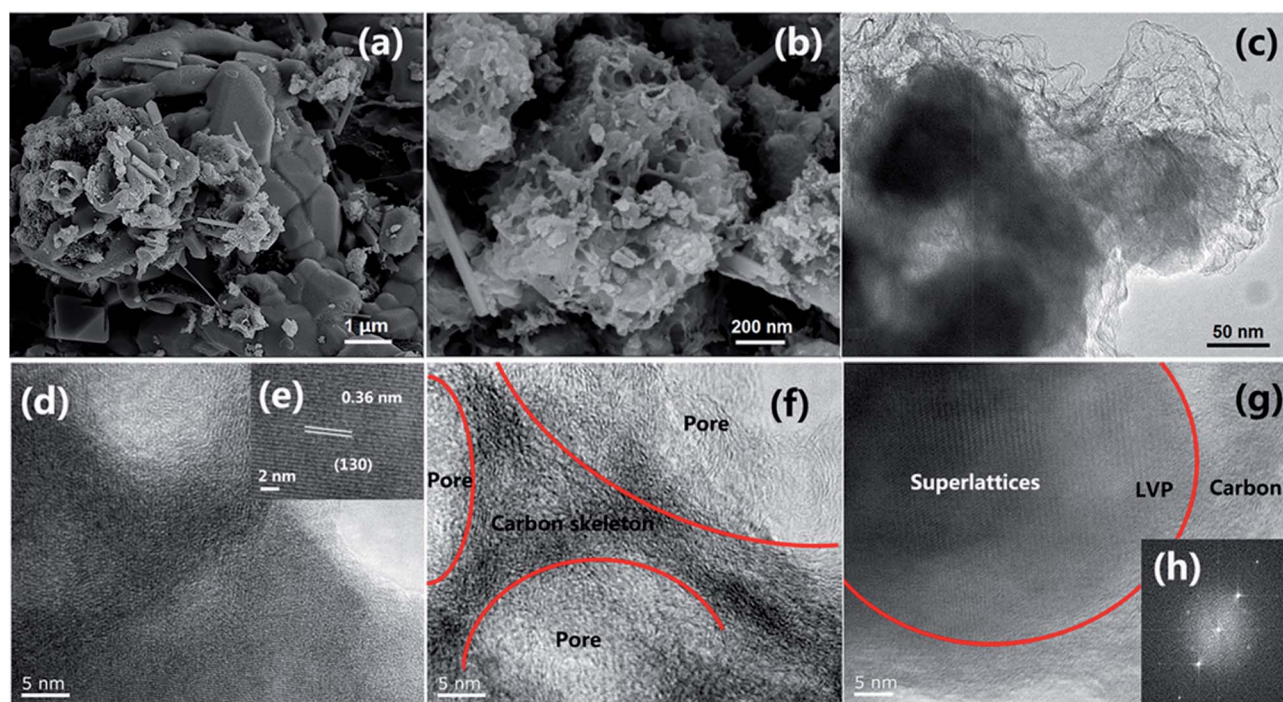


Fig. 2 Structure characterization of LVP/HC-2 sample. (a and b) SEM image. (c) TEM image. (d–g) HRTEM image, and (h) electron diffraction pattern in (g).

clearly see the carbon skeleton and porous structure. In addition, there are some smallish lattice fringes on the carbon. Fig. 2g and h display the super lattice structures in a LVP nanoparticle. SEM images with different magnifications in Fig. 3 show that the pure LVP particles synthesized without using GFLW have no specific morphology and display only non-
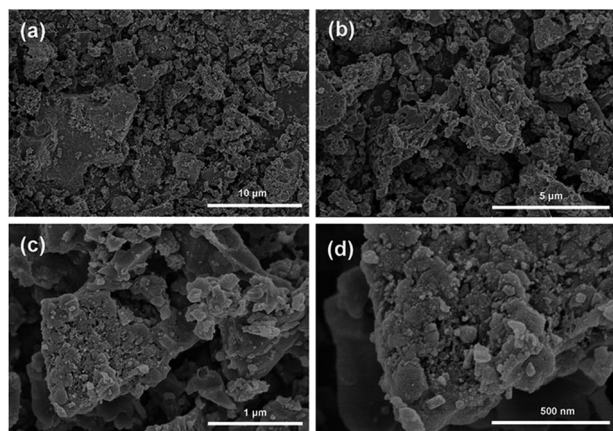
Fig. 3 SEM images of pure LVP synthesized without using GFLW.

uniform hard agglomeration particles. Fig. 4 shows that SEM images of LVP/C-1 sample and LVP/C-3 sample. From Fig. 4a and b we can find that the LVP/C-1 sample is composed of incompact soft agglomeration particles due to the lower heat-treating temperature (750 °C). Because the heat treatment temperature is too high (850 °C), abnormal crystals grow and porous structure collapses, there are many hard agglomeration particles with smooth surface and some large holes in the LVP/C-3 sample (Fig. 4c and d). These agglomeration particles will lead to the poor electrochemical performance of LVP/C-1 and LVP/C-3 samples (Fig. 7a and b). The results show that GFLW and the heat treatment temperature play an important role in the synthesis of 3D porous LVP/HC composites.

The X-ray diffraction (XRD) patterns of the samples synthesized with different calcination temperature are show in Fig. 5a. The XRD data of three samples all showed characteristic diffraction peaks of the monoclinic $Li_3V_2(PO_4)_3$ (JCPDS: 47-0107).[21] Their sharp diffraction peaks indicate that the three samples all have well crystallinity. In addition, a weak peak in green shadow at around 26.5° can be indexed to the characteristic peak of graphite-2H (JCPDS: 41-1487), which can be
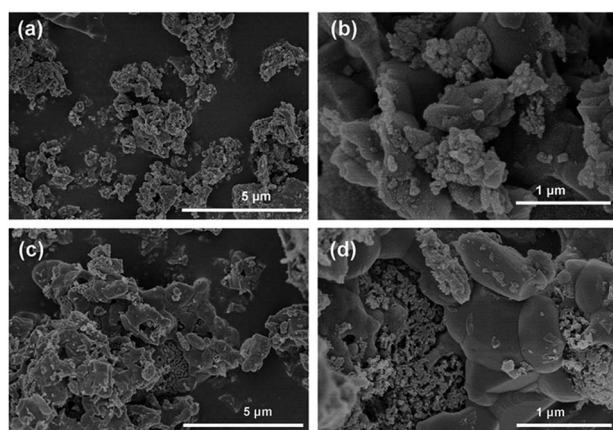
attributed to the graphitization of organic compounds. The crystal structure of LVP is show in Fig. 5b. Each $VO_6$ octahedrons surrounded by six $PO_4$ tetrahedrons, and each $PO_4$ tetrahedrons is surrounded by four $VO_6$ octahedrons, this configuration form a 3D mesh structure space group with the unite of $M_2T_3$, lithium is embedded into the hole of framework. Fig. 5c shows TG curve of the LVP/HC-2 sample in an oxidation atmosphere from room temperature to 1000 °C. According to the previously report,[22,23] the weight loss before 300 °C is attributed to the release of absorbed water and ammonia from the samples. When the temperature rises at the range of 300–500 °C, the weight loss is ascribed to the pyrolysis of surfactant from GFLW. The following weight gain corresponding to the oxidation of $V^{3+}$ in air.[24] According to the TG analysis result, the carbon content in the LVP/HC-2 sample is about 9% in weight percent, and we also set the conditions of heat treatment as below. Firstly, the precursor samples were sintered at 350 °C for 5 h in nitrogen atmosphere to ensure the temperature and time is enough for evaporation of water, ammonia, and the preliminary pyrolysis of organic matter. Then the calcination temperature rise to 800 °C for 8 h in nitrogen atmosphere to gain final sample. Raman spectroscopy is usually used to describe the structure and quality of carbon materials.[25] The typical and deconvoluted Raman spectrum of the LVP/HC-2 sample is shown in Fig. 5d. There are two obvious peaks located at 1360 cm$^{-1}$ (D-peak) and 1595 cm$^{-1}$ (G-peak), respectively, and the D-band is more intensive than the G-band. Generally speaking, the D-peak is used to characterize disordered graphite, the G-peak is related to graphite carbon. The peaks intensity ratio of the G and D band ($I_G/I_D$) provided an index to estimate the crystalline degree and structure of carbon materials.[26] The value of $I_D/I_G$ is calculated to be 1.07, which is very typical for non-graphitic hard carbon materials. The green deconvolution peak in Fig. 5d can be attributable to ionic impurity.[27] The X-ray photoelectron spectroscopy (XPS) is employed to investigate the nature of chemical bonding of the LVP/HC-2 sample. Fig. 5e exhibits the deconvolution results of $V_{2P}$ curves by using two curve-fitting methods with Gaussian function. The peaks located at about 515.7 and 517 eV are attributed to $V^{2+}$ and $V^{3+}$ in the sample, respectively.[28–30] The results from XPS indicate that the LVP in the LVP/HC-2 sample has good structural stability.[31–33] Fig. 5f and show the $N_2$ adsorption–desorption isotherms of the LVP/HC-2 sample, respectively. According to the International Union of Pure and Applied Chemistry Regulation,[34] the isotherm shape of LVP/HC-2 sample in Fig. 5f is the type-III pattern and H3 hysteresis loop, which indicates the presence of non-uniform pores. Its hysteresis loop is attributed to non-uniform pores.[35,36]

Fig. 6a shows the first charge–discharge profiles of the different samples, all of the profiles exhibit three charge/discharge plateaus. The plateaus located around 3.6 V, 3.7 V and 4.1 V are consistent with the monoclinic LVP charge–discharge curve. And obviously, the LVP/HC-2 sample delivers a better discharge capacity. On the other hand, the CV curves of the LVP/HC-2 sample (show in Fig. 6d) are show the charge and discharge process in detail. The rate performance of the LVP/HC-2 sample is shown in Fig. 6b. The battery delivers a superior



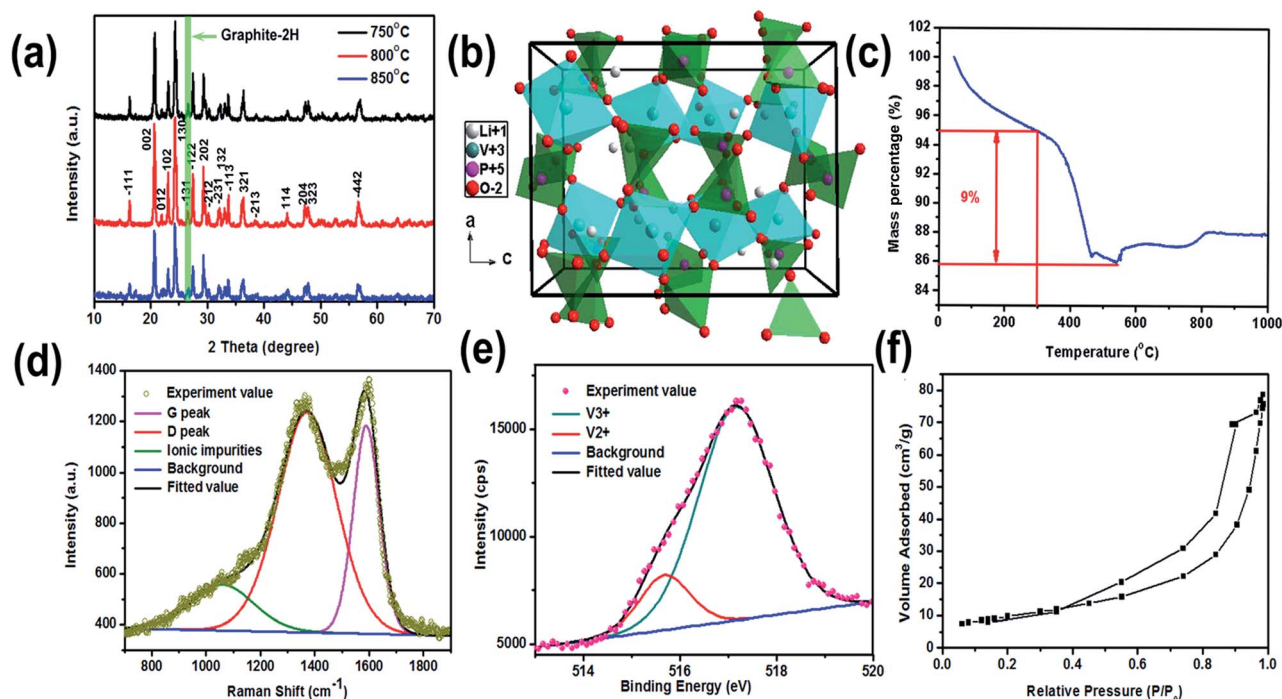Fig. 4 SEM images of LVP/C-1 sample (a and b) and LVP/C-3 sample (c and d).

Fig. 5 Structure characterizations. (a) XRD patterns of the samples synthesized with different calcination temperature, LVP/C-1: 750 °C, LVP/HC-2: 800 °C, LVP/C-3: 850 °C. (b) The crystal structure of LVP. (c) TG curves of the LVP/HC-2 sample in air atmosphere. (d) Raman spectrum of the LVP/HC-2 sample, the D and G peaks are deconvoluted by three-Gaussian peaks. (e) Two-Gaussian peaks fitting deconvolution of high resolution XPS $V_{2p}$ spectrum for LVP/HC-2 sample. (f) The nitrogen adsorption–desorption isotherms of the LVP/HC-2 sample.
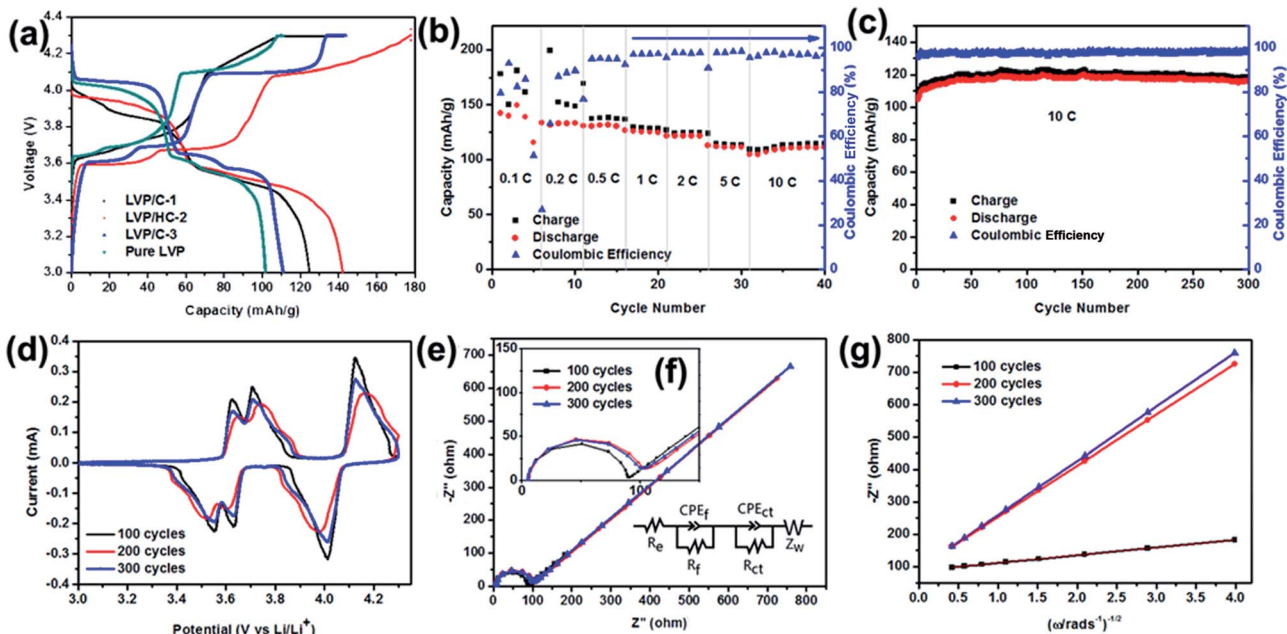


Fig. 6 Electrochemical characterizations of the Li-ion batteries assembled with the samples synthesized with different sintered temperature as a cathode in Li⁺ electrolyte (1 M $LiPF_6$/EC/DC/EMC). LVP/C-1 is the sample sintered at 750 °C, LVP/HC-2 and pure LVP: 800 °C, LVP/C-3: 850 °C. (a) The first charge–discharge curves of different samples tested at 0.1C. (b) Rate performance of LVP/HC-2 cathode from 0.1 to 10C. (c) Cycling performance of LVP/HC-2 at a rate of 10C for 300 cycles. (d) CV curves tested for LVP/HC-2 sample after different cycle numbers at the scan of 0.1 mV s⁻¹ in the voltage range from 3.0 to 4.3 V vs. Li/Li⁺. (e) Nyquist plots of the LVP/HC-2 cathode tested at different cycle numbers at 10C between 3.0–4.3 V vs. Li/Li⁺ (inset: the equivalent circuit used to fit the EIS). (f) Is the enlarged Nyquist plots. (g) The plots of impedance as a function of the inverse square root of angular frequency in the low frequency region.

electrochemical capacity of 142 mA h g$^{-1}$ at 0.1C, which is exceeded the theoretical capacity of monoclinic LVP (133 mA h g$^{-1}$). Even at the rate of 10C also could obtain a capacity above 110 mA h g$^{-1}$. This is attribute to three structural advantages of the LVP/HC-2 sample. Firstly, the LVP nanocrystallines with the

superlattice structures have abundant reactive sites of electron and Li$^+$ in the quantum wells due to quantum confinement and size effects. Secondly, the electrochemically active HC can be uniformly coated on the surface of LVP nanoparticles and effectively store Li ions in its porous network structure. This can not only suppress the aggregation of LVP particles in the synthesis to increase contact area with electrolyte and improve lithium ion transport, but also accommodate the volume change during the cycling processes to enhance its rate performance and cycle stability. Third, the unique nanocomposite structure gives a remarkable synergy effect for both ion storage and electrochemical kinetics, hence the sample exhibit remarkable electrochemical performances in lithium ion batteries. Fig. 6c shows the cycling performance of the LVP/HC-2 cathode at the rate of 10C in the voltage range of 3.0–4.3 V vs. Li/Li$^+$. The maximum specific discharge capacity is 120.1 mA h g$^{-1}$ and can retain of 96.34% of capacity after 300 cycles. The coulombic efficiency is above 97% during the cycling process, demonstrating the excellent reversibility of the LVP/HC-2 sample. Fig. 7 shows the rate performances of different samples from 0.1C to 10C. Compared with Fig. 5b, the rate performances of LVP/C-1 (Fig. 7a), LVP/C-3 (Fig. 7b) and pure LVP (Fig. 7c) cathodes are all poor, and its discharge capacity tends to obviously decrease, especially after 5C, but its coulombic efficiency remains above 97% during the cycling process. Table 1 shows the comparison of electrochemical performances of the LVP cathodes with different morphology. The results of comparison show that the LVP/HC-2 cathode can greatly improve the performances and the coulombic efficiency of LIBs at high rate.

The CV curves obtained for LVP/HC-2 sample after different cycle numbers (show in Fig. 6d) are used to understand the electrochemical process. It is obvious that the first 100 cycles have the sharpest peaks, the second 100 cycles the intensity of peak became lower and following 100 cycles increased again, indicating polarization and kinetics for Li ions insertion/extraction turn to the steady state.[33] The homologous electrochemical impedance spectroscopy (EIS) was performed to investigate the Li$^+$ diffusion in the process of circulation (Fig. 6e and f). It is clear that the three Nyquist plots are all composed of arcs at high and middle frequencies region and a slanted line in the low frequency region.[37] The diameter of the arc is correlated with the charge transfer resistance ($R_{ct}$) and constant phase element. The slanted line is attributed to the Warburg
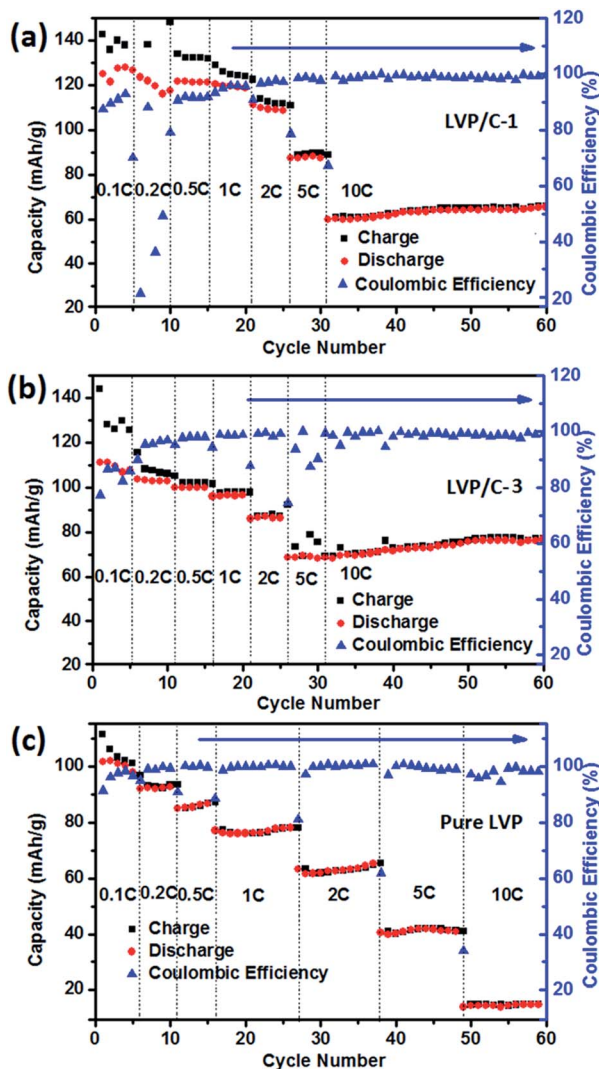


Fig. 7 Rate performances of different samples from 0.1C to 10C. (a) LVP/C-1, (b) LVP/C-3 and (c) pure LVP.

Table 1 Comparison of electrochemical performances of the LVP cathodes with different morphology

| Samples | Initial discharge capacities [mA h g$^{-1}$] | Morphology | Charge potentials | References in the text |
|---|---|---|---|---|
| LVP/C-1 | 125 (0.1C), 60 (10C) | Block | 3.0–4.3 V | The text |
| LVP/HC-2 | 143 (0.1C), 92 (10C) | Porous structure | 3.0–4.3 V | The text |
| LVP/C-3 | 111 (0.1C), 68 (10C) | Block | 3.0–4.3 V | The text |
| Pure LVP | 102 (0.1C), 14 (10C) | Bulk | 3.0–4.3 V | The text |
| Li$_3$V$_2$(PO$_4$)$_3$/C | 125 (1C), 118 (10C) | Bulk | 3.0–4.3 V | Ref. 40 |
| Li$_3$V$_{1.94}$Fe$_{0.06}$(PO$_4$)$_3$/C | 164 (1C), 129 (5C) | Irregular | 3.0–4.8 V | Ref. 41 |
| Li$_3$V$_2$(PO$_4$)$_3$/C | 128 (0.5C), 120 (10C) | Nanofiber | 3.0–4.3 V | Ref. 42 |
| Li$_3$V$_2$(PO$_4$)$_3$/rGO&C | 109 (20C), 63 (100C) | Sheet | 3.0–4.3 V | Ref. 8 |
| Na$_3$V$_2$(PO$_4$)$_3$/C | 131 (0.5C), 112 (10C) | Microsphere | 3.0–4.3 V | Ref. 21 |

**Table 2** The change of the electrochemical performances for the LVP/HC-2 cathode after different cycle numbers at 10C between 3.0–4.3 V vs. Li/Li$^+$ at room temperature

| Cycle number | $R_{ct}$ (Ω) | $\sigma$ | $C$ (mol cm$^{-3}$) | $D$ (cm$^2$ s$^{-1}$) |
|---|---|---|---|---|
| 100 | 88.5 | 23.70 | $1.5 \times 10^{-2}$ | $5.6 \times 10^{-15}$ |
| 200 | 114.6 | 157.6 | $1.5 \times 10^{-2}$ | $1.3 \times 10^{-16}$ |
| 300 | 113.0 | 166.9 | $1.5 \times 10^{-2}$ | $1.1 \times 10^{-16}$ |

impedance ($Z_W$) which is related to Li ion diffusion in the active materials.[38] The equivalent circuit is shown in Fig. 6e. In the equivalent circuit, $R_e$ and $R_f$ represent the ohmic resistance of whole reaction system, which contains the electrolyte resistance, inter-particle contact resistance and other physical resistances between the electrolyte and electrode. CPE is the double layer capacitance on the electrode surface.

Fig. 6g shows the linear fitting of $Z_{real}$ vs. $\omega^{-1/2}$, from which the slope $\sigma$ can be obtained. Using this $\sigma$ value it is possible to calculate the lithium diffusion coefficients of the material.[39–44] The change of the electrochemical performances of LVP/HC-2 cathode after different cycle numbers at 10C given in Table 1 at room temperature. The concentration of lithium ion ($C$) was calculated by the following equation:

$$C = \frac{n_{Li}}{N_A V} \tag{1}$$

where $n_{Li}$ is the number of Li$^+$ in each LVP unit cell ($n_{Li} = 8$), $N_A$ is Avogadro's constant ($N_A = 6.05 \times 10^{23}$ mol$^{-1}$), $V$ is the unit cell volume of LVP estimated by Jade 5.0 (88.75 nm$^3$).

Eqn (2) was employed to calculated the lithium ion diffusion coefficient. Where $R$ is the gas constant ($R = 8.314$ J mol$^{-1}$ K$^{-1}$), $T$ is the temperature ($T = 298.15$ K), $A$ is the area of the electrode surface ($A = 1.76$ cm$^2$), $n$ is the number of electrons per molecule during oxidization ($n = 2$), $F$ is Faraday's constant ($F = 96\,486$ C mol$^{-1}$), $\sigma$ is the Warburg factor which is obtained from eqn (3), $\omega$ is angle frequency.[21] All the results listed in Table 2.

$$D = \frac{R^2 T^2}{2A^2 n^4 F^4 C^2 \sigma^2} \tag{2}$$

$$Z_{real} = R_e + R_{ct} + \sigma \omega^{-1/2} \tag{3}$$

Fig. 8 delivers the long life performance of LVP/HC-2 cathode at the rate of 10C. The initial capacity decreases to 98 mA h g$^{-1}$ after 1000 cycles and the corresponding capacity retention is
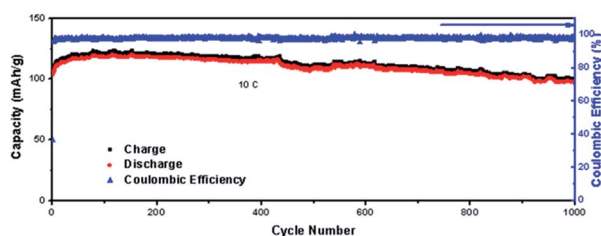


**Fig. 8** Cycling performance of LVP/HC-2 at a high rate of 10C for 1000 cycles.

82%. This results indicate that the non-uniform pores LVP/HC-2 cathode material is a very potential candidate for high rate and long life Li-ion batteries.

# 4. Conclusions

We have demonstrated the feasible of sol–gel method to synthesize non-uniform pores Li$_3$V$_2$(PO$_4$)$_3$ (LVP)/hard carbon (HC) cathode material. This special three dimensional (3D) architecture provides transfer pathways for Li ion more effectively and rapidly. A specific capacity of 142 mA h g$^{-1}$ can be acquired at 0.1C. When the rate rise to 10C, a maximum specific capacity of 120 mA h g$^{-1}$ can be obtained and capacity retention can reach 82% after 1000 cycles. The 3D-LVP/HC with prominent rate and long lifespan performances is a great potential cathode for Li-ion batteries. Simultaneously, the experiment used a large number of GFLW as the raw material, achieved the purpose of recycling waste which is positive in environmental protection.

# Acknowledgements

# Notes and references

1 M. Armand and J. M. Tarascon, *Nature*, 2008, **451**, 652–657.
2 S. Chu and A. Majumdar, *Nature*, 2012, **488**, 294–303.
3 R. Lee, *Science*, 2011, **333**, 569–573.
4 J. Yan, Y. C. Cao and F. J. Liu, *RSC Adv.*, 2016, **6**, 113228–113233.
5 H. Wu, Z. Wang, S. Liu, L. Zhang and Y. Zhang, *ChemElectroChem*, 2015, **2**, 1921–1928.
6 X. C. Tian, X. Xu, L. He, Q. L. Wei, M. Y. Yan, L. Xu, Y. L. Zhao, C. C. Yang and L. Q. Mai, *J. Power Sources*, 2014, **255**, 235–241.
7 Y. Xia, Z. Xiao, X. Dou, H. Huang, X. H. Lu, R. J. Yan, Y. P. Gan, W. J. Zhu, J. P. Tu, W. K. Zhang and X. Y. Tao, *ACS Nano*, 2013, **7**, 7083–7092.
8 Q. L. Wei, Y. N. Xu, Q. D. Li, S. S. Tan, W. H. Ren, Q. Y. An and L. Q. Mai, *Chem. Commun.*, 2016, **52**, 8730–8732.
9 S. Kim, Z. X. Zhang, S. L. Wang, L. Yang, E. J. Cairns, J. E. P. Hahn and A. Deb, *J. Phys. Chem. C*, 2016, **120**, 7005–7012.
10 L. L. Zhang, H. B. Sun, X. L. Yang, M. Li, Z. Li, S. B. Ni and H. C. Tao, *J. Solid State Electrochem.*, 2016, **20**, 311–318.
11 S. Q. Liang, X. X. Cao, Y. P. Wang, Y. Hu, A. Q. Pan and G. Z. Cao, *Nano Energy*, 2016, **22**, 48–58.
12 W. C. Duan, Z. Hu, K. Zhang, F. Y. Cheng, Z. L. Tao and J. Chen, *Nanoscale*, 2013, **5**, 6485–6490.

13 X. Y. Cao, P. Ge, L. M. Zhu, L. L. Xie, Z. H. Yu, J. J. Zhang, X. L. Cao and S. Y. Xiong, *Int. J. Electrochem. Sci.*, 2016, **11**, 5217–5225.

14 X. H. Nan, C. K. Zhang, C. F. Liu, M. M. Liu, Z. L. Wang and G. Z. Cao, *ACS Appl. Mater. Interfaces*, 2016, **8**, 862–870.

15 L. Q. Mai, S. Li, Y. F. Dong, Y. L. Zhao, Y. Z. Luo and H. M. Xu, *Nanoscale*, 2013, **5**, 4864–4869.

16 J. T. Xu, M. Wang, N. P. Wickramaratne, M. Jaroniec, S. X. Dou and L. M. Dai, *Adv. Mater.*, 2015, **27**, 2042–2048.

17 Y. P. Zhou, X. H. Rui, W. P. Sun, Z. C. Xu, Y. Zhou, W. J. Ng, Q. Y. Yan and E. Fong, *ACS Nano*, 2015, **9**, 4628–4635.

18 L. F. Shen, J. Wang, C. Y. Xu, H. S. Li, H. Dou and X. G. Zhang, *Adv. Energy Mater.*, 2015, **5**, 1400977–1400983.

19 K. Z. Cao, L. F. Jiao, H. Q. Liu, Y. C. Liu, Y. J. Wang, Z. P. Guo and H. T. Yuan, *Adv. Energy Mater.*, 2015, **5**, 4646–4652.

20 R. P. Fang, S. Y. Zhao, P. X. Hou, M. Cheng, S. G. Wang, H. M. Cheng, C. Liu and F. Li, *Adv. Mater.*, 2016, **28**, 3374–3382.

21 Y. Z. Luo, X. Xu, Y. X. Zhang, Y. Q. Pi, C. H. Han, M. Y. Yan, Q. L. Wei and L. Q. Mai, *Sci. Lett.*, 2015, **4**, 130–135.

22 Y. Q. Qiao, J. P. Tu, X. L. Wang and C. D. Gu, *J. Power Sources*, 2012, **199**, 287–292.

23 X. H. Rui, C. Li and C. H. Chen, *Electrochim. Acta*, 2009, **54**, 3374–3380.

24 C. L. Wei, W. He, X. D. Zhang, S. J. Liu, C. Jin, S. K. Liu and Z. Huang, *RSC Adv.*, 2015, **5**, 28662–28669.

25 A. Das, S. Pisana, B. Chakraborty, S. Piscanec, S. K. Saha, U. V. Waghmare, K. S. Novoselov, H. R. Krishnamurthy, A. K. Geim, A. C. Ferrari and A. K. Sood, *Nat. Nanotechnol.*, 2008, **3**, 210–215.

26 D. H. Seo, A. E. Rider, Z. J. Han, S. Kumar and K. K. Ostrikov, *Adv. Mater.*, 2013, **25**, 5638–5642.

27 Y. X. Ding, X. Y. Sun, L. Y. Zhang, S. J. Mao, Z. L. Xie, Z. W. Liu and D. S. Su, *Angew. Chem., Int. Ed.*, 2015, **54**, 231–235.

28 D. W. Han, S. J. Lim, Y. I. Kim, S. H. Kang, Y. C. Lee and Y. M. Kang, *Chem. Mater.*, 2014, **26**, 3644–3650.

29 M. M. Ren, Z. Zhou, Y. Z. Li, X. P. Gao and J. Yan, *J. Power Sources*, 2006, **162**, 1357–1362.

30 Y. S. Chen, D. Zhang, X. F. Bian, X. F. Bie, C. Z. Wang, F. Du, M. Jang, G. Chen and Y. J. Wei, *Electrochim. Acta*, 2012, **79**, 95–101.

31 A. W. Moses, G. H. G. Flores, J. G. Kim and M. A. Langell, *Appl. Surf. Sci.*, 2007, **253**, 4782–4791.

32 R. Dedryvere, M. Maccario, L. Croguennec, F. L. Cras, C. Delmas and D. Gonbeau, *Chem. Mater.*, 2008, **20**, 7164–7170.

33 W. C. Duan, Z. Hu, K. Zhang, F. Y. Cheng, Z. L. Tao and J. Chen, *Nanoscale*, 2013, **5**, 6485–6490.

34 R. R. Xu, W. Q. Pang, J. H. Yu, Q. S. Huo and J. S. Chen, *Chemistry-Zeolites and Porous Materials*, Science Press, 2004, pp. 146–158.

35 A. Sayari and S. Hamoudi, *Chem. Mater.*, 2001, **13**, 3151–3168.

36 M. Kruk and M. Jaroniec, *Chem. Mater.*, 2001, **13**, 3169–3183.

37 H. X. Ji, L. L. Zhang, M. T. Pettes, H. F. Li, S. S. Chen, L. Shi, R. Piner and R. S. Ruoff, *Nano Lett.*, 2012, **12**, 2446–2451.

38 X. L. Wu, Y. G. Guo, J. Su, J. W. Xiong, Y. L. Zhang and L. J. Wan, *Adv. Energy Mater.*, 2013, **3**, 1155–1160.

39 J. Liu, P. J. Lu, S. Q. Liang, J. Liu, W. J. Wang, M. Lei, S. S. Tang and Q. Yang, *Nano Energy*, 2015, **12**, 709–724.

40 P. J. Lu, M. Lei and J. Liu, *CrystEngComm*, 2014, **16**, 6745–6755.

41 J. S. Luo, X. H. Xia, Y. S. Luo, C. Guan, J. L. Liu, X. J. Qi, C. F. Ng, T. Yu, H. Zhang and H. J. Fan, *Adv. Energy Mater.*, 2013, **3**, 737–743.

42 J. Yan, Y. C. Cao and F. J. Liu, *RSC Adv.*, 2016, **6**, 113228–113233.

43 Z. Li, L. L. Zhang, X. L. Yang, H. B. Sun, Y. H. Huang and G. Liang, *RSC Adv.*, 2016, **6**, 10334–10340.

44 P. P. Sun, X. Y. Zhao, R. P. Chen, T. Chen, L. B. Ma, Q. Fan, H. L. Lu, Y. Hu, Z. X. Tie, Z. Jin, Q. Y. Xu and J. Liu, *Nanoscale*, 2016, **8**, 7408–7415.